Semantic Attention Flow Fields for Monocular Dynamic Scene Decomposition

Yiqing Liang Eliot Laidlaw Alexander Meyerowitz Srinath Sridhar James Tompkin
Brown University

Abstract

From video, we reconstruct a neural volume that captures time-varying color, density, scene flow, semantics, and attention information. The semantics and attention let us identify salient foreground objects separately from the background across spacetime. To mitigate low resolution semantic and attention features, we compute pyramids that trade detail with whole-image context. After optimization, we perform a saliency-aware clustering to decompose the scene. To evaluate real-world scenes, we annotate object masks in the NVIDIA Dynamic Scene and DyCheck datasets. We demonstrate that this method can decompose dynamic scenes in an unsupervised way with competitive performance to a supervised method, and that it improves foreground/background segmentation over recent static/dynamic split methods.
Project webpage: https://visual.cs.brown.edu/saff

1. Introduction

Given a casually-captured monocular RGB video of a dynamic scene, decomposing it into foreground objects and background is an important task in computer vision, with downstream applications in segmentation and video editing. An ideal method would also reconstruct the geometry and appearance over time including frame correspondences.

Previous methods have made great progress but there are many limitations. Some works assume that there is no object motion in the scene [39, 52, 38, 18, 4], take input from multi-view cameras [18, 52], or do not explicitly reconstruct the underlying 3D structure of the scene [4, 8]. For objects, some works rely on masks or user input to aid segmentation [48, 17, 8], or use task-specific training datasets [8]. Sometimes, works assume the number of foreground objects [4, 25]. Given the challenges, many works train and test on synthetic data [16, 45].

We present Semantic Attention Flow Fields (SAFF): A method to overcome these limitations by integrating low-level reconstruction cues with high-level pretrained information—both bottom-up and top-down—into a neural volume. With this, we demonstrate that embedded semantic and saliency (attention) information is useful for unsupervised dynamic scene decomposition. SAFF builds upon neural scene flow fields [22], an approach that reconstructs appearance, geometry, and motion. This uses frame interpolation rather than explicit canonicalization [42] or a latent hyperspace [33],

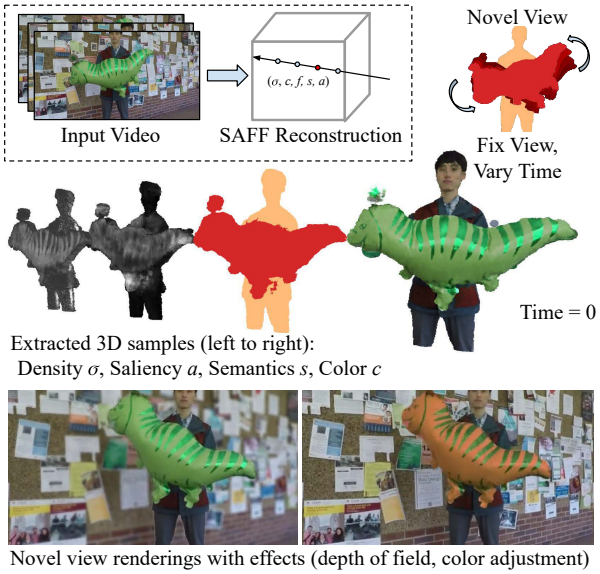

Figure 1: We decompose a dynamic 3D scene from monocular input into time-varying color, density, scene flow, semantics, and attention information. This could be used to provide precise editing of objects or effects focused around objects.

which lets it more easily apply to casual videos. For optimization, we supervise two network heads with pretrained DINO-ViT [6] semantic features and attention. Naively supervising high-resolution SAFF with low-resolution DINO-ViT output reduces reconstruction quality. To mitigate the mismatch, we build a semantic attention pyramid that trades detail with whole-image context. Having optimized a SAFF representation for a dynamic scene, we perform a saliency-aware clustering both in 3D and on rendered feature images to describe objects and their background. Given the volume reconstruction, the clustering generalizes to novel spacetime views.

To evaluate SAFF's dynamic scene decomposition capacity, we expand the NVIDIA Dynamic Scene [51] and DyCheck [11] datasets by manually annotating object masks across input and hold-out views. We demonstrate that SAFF outperforms 2D DINO-ViT baselines and is comparable to a state-of-the-art video segmentation method ProposeReduce[24] on our data. Existing monocular video dynamic volume reconstruction methods typically separate static and dynamic parts, but these often do not represent meaningful foreground. We show improved foreground segmentation over NSFF and the current D^{2}NeRF [47] method for downstream tasks like editing.

2. Related Work

Decomposing a scene into regions of interest is a long-studied task in computer vision [5], including class, instance, and panoptic segmentation in high-level or top-down vision, and use of low-level or bottom-up cues like motion. Recent progress has considered images [13, 4, 25], videos [16, 17], layer decomposition [50, 29], and in-the-wild databases using deep generative models [31]. One example, SAVi++[8], uses slot attention [25] to define 2D objects in real-world videos. Providing first-frame segmentation masks achieves stable performance, with validation on the driving Waymo Open Dataset [40]. Our work attempts 3D scene decomposition for a casual monocular video without initial masks.

Scene Decomposition with NeRFs Neural Radiance Fields (NeRF) [**?**] have spurred new scene decomposition research through volumes. ObSuRF [39] and uORF [52] are unsupervised slot attention works that bind a latent code to each object. Unsupervised decomposition is also possible on light fields [38]. For dynamic scenes, works like NeuralDiff [44] and D^{2}NeRF [47] focus on foreground separation, where foreground is defined to contain moving objects. Other works like N3F [43] and occlusions-4d [14] also decompose foregrounds into individual objects. N3F requires user input to specify which object to segment, and occlusions-4d takes RGB point clouds as input. Our work attempts to recover a segmented dynamic scene from a monocular RGB video without added markup or masks.

Neural Fields Beyond Radiance Research has begun to add non-color information to neural volumes to aid decomposition via additional feature heads on the MLP. iLabel [54] adds a semantic head to propagate user-provided segmentations in the volume. PNF [21] and Panoptic-NeRF [10] attempt panoptic segmentation within neural fields, and Object-NeRF integrates instance segmentation masks into the field during optimization [48]. Research also investigates how to apply generic pretrained features to neural fields, like DINO-ViT.

DINO-ViT for Semantics and Saliency DINO-ViT is a self-supervised transformer that, after pretraining, extracts generic semantic information [6]. Amir et al. [1] use DINO-ViT features with k-means clustering to achieve co-segmentation across a video. Seitzer et al. [36] combine slot attention and DINO-ViT features for object-centric learning on real-world 2D data. TokenCut [46] performs normalized cuts on DINO-ViT features for foreground segmentation on natural images. Deep Spectral Segmentation [27] show that graph Laplacian processing of DINO-ViT features provides unsupervised foreground segmentation, and Selfmask [37] shows that these features can provide object saliency masks. Our approach considers these clustering and saliency findings for the setting of 3D decomposition from monocular video.

DINO-ViT Fields Concurrent works have integrated DINO-ViT features into neural fields. DFF [18] distills features for dense multi-view static scenes with user input for segmentation. N3F [43] expands NeuralDiff to dynamic scenes, and relies on user input for segmentation. AutoLabel [3] uses DINO-ViT features to accelerate segmentation in static scenes given a ground truth segmentation mask. Other works use DINO-ViT differently. FeatureRealistic-Fusion [26] uses DINO-ViT in an online feature fusion task, focusing on propagating user input, and NeRF-SOS [9] uses 2D DINO-ViT to process NeRF-rendered multi-view RGB images of a static scene. In contrast to these works, we consider real-world casual monocular videos, recover and decompose a 3D scene, then explore whether saliency can avoid the need for masks or user input in segmenting objects.

3. Method

For a baseline dynamic scene reconstruction method, we begin with NSFF from Li *et al*. [22] (Sec. 3.1), which builds upon NeRF [28]. NSFF's low-level scene flow frame-to-frame approach provides better reconstructions for real-world casual monocular videos than deformation-based methods [42, 33]. We modify the architecture to integrate higher-level semantic and saliency (or attention) features (Sec. 3.2). After optimizing a SAFF for each scene, we perform saliency-aware clustering of the field (Sec. 3.4). All implementation details are in our supplemental material.

Input Our method takes in a single RGB video over time i as an ordered set of images $I \in \mathcal{I}$ and camera poses. We use COLMAP to recover camera poses [35]. From all poses, we define an NDC-like space that bounds the scene, and a set of rays $\mathbf{r} \in \mathcal{R}$, one per image pixel with color $\hat{\mathbf{c}}^\dagger$. Here, $\hat{\cdot}$ denotes a 2D pixel value in contrast to a 3D field value, and $\cdot^\dagger$ denotes an input value in contrast to an estimated value.

From pretrained networks, we estimate single-frame monocular depth $\hat{d}^\dagger$ (MiDaSv2 [34]), optical flow $\hat{\mathbf{p}}_i^\dagger$ (RAFT [41]), and semantic features $\hat{\mathbf{s}}^\dagger$ and attention $\hat{\mathbf{a}}^\dagger$ (DINO-ViT [6]) after important preprocessing (Sec. 3.3).

3.1. Initial Dynamic Neural Volume Representation

The initial representation comprises a static NeRF $F_{\boldsymbol{\theta}}^{\text{st}}$ and a dynamic NeRF $F_{\boldsymbol{\theta}}^{\text{dy}}$. The static network predicts a color $\mathbf{c}$, density σ, and blending weight v (Eq. (1)), and the dynamic network predicts time-varying color $\mathbf{c}_i$, density σ_i, scene flow $\mathbf{f}_i$, and occlusion weights w_i (Eq. (2)). In both network architectures, other than position $\mathbf{x}$, we add direction $\boldsymbol{\omega}$ to a late

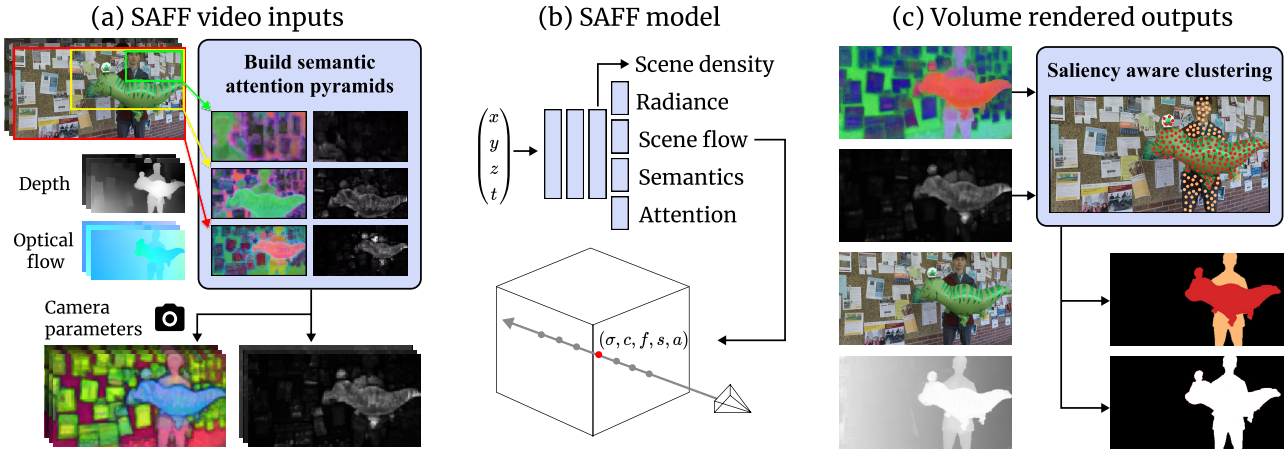

Figure 2: **Overview.** From monocular video, SAFF builds a neural field of scene-flowed 3D density, radiance, semantics, and attention (b). This is guided by semantic attention pyramids that increase resolution, plus depth and optical flow priors (a). We can render new spacetime views of any channel, and use saliency-aware clustering to decompose objects and background (c).

separate head to only condition the estimation of color $\mathbf{c}$.

$$F_{\boldsymbol{\theta}}^{\text{st}} : (\mathbf{x}, \boldsymbol{\omega}) \quad \rightarrow (\mathbf{c}^{\text{st}}, \sigma^{\text{st}}, v) \tag{1}$$

$$F_{\boldsymbol{\theta}}^{\text{dy}} : (\mathbf{x}, \boldsymbol{\omega}, i) \rightarrow (\mathbf{c}_i^{\text{dy}}, \sigma_i^{\text{dy}}, \mathbf{f}_i, w_i) \tag{2}$$

To produce a pixel's color, we sample points at distances t along the ray $\mathbf{x}_t = \mathbf{x} - \boldsymbol{\omega} t$ between near and far planes t_n to t_f, query each network, then integrate transmittance T, density σ, and color along the ray from these samples [28]. For brevity, we omit evaluating at $\mathbf{x}_t, \boldsymbol{\omega}$, *e.g.*, $\sigma^{\text{st}}(\mathbf{x}_t)$ is simply σ^{st}; $\mathbf{c}^{\text{st}}(\mathbf{x}_t, \boldsymbol{\omega})$ is simply $\mathbf{c}^{\text{st}}$.

We produce a combined color from the static and dynamic colors by multiplication with their densities:

$$\sigma_i \mathbf{c}_i = v \sigma^{\text{st}} \mathbf{c}^{\text{st}} + (1 - v) \sigma_i^{\text{dy}} \mathbf{c}_i^{\text{dy}} \tag{3}$$

Given that transmittance integrates density up to the current sampled point under Beer-Lambert volume attenuation, the rendered pixel color for the ray is computed as:

$$\hat{\mathbf{c}}_i = \int_{t_n}^{t_f} T_i \sigma_i \mathbf{c}_i \, dt \quad \text{where} \quad T_i = \exp\left(- \int_{t_n}^{t} \sigma_i \, dt \right) \tag{4}$$

To optimize the volume to reconstruct input images, we compute a photometric loss $L_{\hat{\mathbf{c}}}$ between rendered and input colors:

$$\mathcal{L}_{\hat{\mathbf{c}}} = \frac{1}{|\mathcal{R}|} \sum_{\mathbf{r}_i \in \mathcal{R}} ||\hat{\mathbf{c}}_i(\mathbf{r}_i) - \hat{\mathbf{c}}_i^{\dagger}(\mathbf{r}_i)||_2^2 \tag{5}$$

Scene Flow Defining correspondence over time is important for monocular input as it lets us penalize a reprojection error with neighboring frames $j \in \mathcal{N}$, e.g., where $j = i + 1$ or $j = i - 1$. We denote $_{i \rightarrow j}$ for the projection of frame i onto frame j by scene flow. $F_{\boldsymbol{\theta}}^{\text{dy}}$ estimates both forwards and backwards scene flow at every point to penalize a bi-direction loss.

Thus, we approximate color output at time step j by flowing the queried network values at time step i:

$$\hat{\mathbf{c}}_{i \rightarrow j} = \int_{t_n}^{t_f} T_{i \rightarrow j} \sigma_{i \rightarrow j} \mathbf{c}_{i \rightarrow j} \, dt \tag{6}$$

Reprojection must account for occlusion and disocclusion by motion. As such, $F_{\boldsymbol{\theta}}^{\text{dy}}$ also predicts forwards and backwards scene occlusion weights w_{i+1} and $w_{i-1} \in [0, 1]$, where a point with $w_{i+1} = 0$ means that occlusion status is changed one step forwards in time. We can integrate w to a pixel:

$$\hat{w}_{i \rightarrow j} = \int_{t_n}^{t_f} T_{i \rightarrow j} \sigma_{i \rightarrow j} w_j \, dt \tag{7}$$

Then, this pixel weight modulates the color loss such that occluded pixels are ignored.

$$\mathcal{L}_{\hat{\mathbf{c}}_{i \rightarrow j}} = \frac{1}{|\mathcal{R}||\mathcal{N}|} \sum_{\mathbf{r}_i \in \mathcal{R}} \sum_{j \in \mathcal{N}} \hat{w}_{i \rightarrow j}(\mathbf{r}_i) ||\hat{\mathbf{c}}_{i \rightarrow j}(\mathbf{r}_i) - \hat{\mathbf{c}}_j^{\dagger}(\mathbf{r}_j)||_2^2 \tag{8}$$

Prior losses We use the pretrained depth and optical flow map losses to help overcome the ill-posed monocular reconstruction problem. These losses decay as optimization progresses to rely more and more on the optimized self-consistent geometry and scene flow. For geometry, we estimate a depth $\hat{d}_i$ for each ray $\mathbf{r}_i$ by replacing $\mathbf{c}_i$ in Eq. (4) by the distance t along the ray. Transform z estimates a scale and shift as the pretrained network produces only relative depth.

$$\mathcal{L}_{\hat{d}} = \frac{1}{|\mathcal{R}|} \sum_{\mathbf{r}_i \in \mathcal{R}} ||\hat{d}_i - z(\hat{d}_i^{\dagger})||_1 \tag{9}$$

For motion, projecting scene flow to a camera lets us compare to the estimated optical flow. Each sample point along a ray $\mathbf{x}_i$ is advected to a point in the neighboring frame $\mathbf{x}_{i \rightarrow j}$, then integrated to the neighboring camera plane to produce a 2D

point offset $\hat{\mathbf{p}}_i(\mathbf{r}_i)$. Then, we expect the difference in the start and end positions to match the prior:

$$\mathcal{L}_{\hat{\mathbf{p}}} = \frac{1}{|\mathcal{R}||\mathcal{N}|} \sum_{\mathbf{r}_i \in \mathcal{R}} \sum_{j \in \mathcal{N}(i)} ||\hat{\mathbf{p}}_i(\mathbf{r}_i) - \hat{\mathbf{p}}_i^{\dagger}(\mathbf{r}_i)||_1 \quad (10)$$

Additional regularizations encourage occlusion weights to be close to one, scene flow to be small, locally constant, and cyclically consistent, and blending weight v to be sparse.

3.2. Semantic Attention Flow Fields

Beyond low-level or *bottom-up* features, high-level or *top-down* features are also useful to define objects and help down-stream tasks like segmentation. For example, methods like NSFF or D^{2}NeRF struggle to provide *useful* separation of static and dynamic parts because blend weight v estimates whether the volume *appears* to be occupied by some moving entity. This is not the same as objectness; tasks like video editing could benefit from accurate dynamic object masks.

As such, we extract 2D semantic features and attention (or saliency) values from a pretrained DINO-ViT network, then optimize the SAFF such that unknown 3D semantic and attention features over time can be projected to recreate their 2D complements. This helps us to ascribe semantic meaning to the volume and to identify objects. As semantics/attention are integrated into the 4D volume, we can render them from novel spacetime views without further DINO-ViT computation.

To estimate semantic features $\mathbf{s}$ and attention $\mathbf{a}$ at 3D points in the volume at time i, we add two new heads to both the static $F_{\boldsymbol{\theta}}^{\text{st}}$ and the dynamic $F_{\boldsymbol{\theta}}^{\text{dy}}$ networks:

$$F_{\boldsymbol{\theta}}^{\text{st}} : (\mathbf{x}, \boldsymbol{\omega}) \quad \rightarrow (\mathbf{c}^{\text{st}}, \sigma^{\text{st}}, v, \mathbf{s}^{\text{st}}, \mathbf{a}^{\text{st}}) \quad (11)$$

$$F_{\boldsymbol{\theta}}^{\text{dy}} : (\mathbf{x}, \boldsymbol{\omega}, i) \rightarrow (\mathbf{c}_i^{\text{dy}}, \sigma_i^{\text{dy}}, \mathbf{f}_i, w_i, \mathbf{s}_i^{\text{dy}}, \mathbf{a}_i^{\text{dy}}) \quad (12)$$

As semantic features have been demonstrated to be somewhat robust to view dependence [1], in our architectures both heads for $\mathbf{s}$, $\mathbf{a}$ are taken off the backbone before $\boldsymbol{\omega}$ is injected.

To render semantics from the volume, we replace the color term $\mathbf{c}$ in Eq. (4) with $\mathbf{s}$ and equivalently for $\mathbf{a}$:

$$\sigma_i \mathbf{s}_i = v\sigma^{\text{st}}\mathbf{s}^{\text{st}} + (1-v)\sigma_i^{\text{dy}}\mathbf{s}_i^{\text{dy}}, \; \hat{\mathbf{s}}_i = \int_{t_n}^{t_f} T_i \sigma_i \mathbf{s}_i \, dt \quad (13)$$

To encourage scene flow to respect semantics over time, we penalize complementary losses on $\mathbf{s}$ and $\mathbf{a}$ (showing $\mathbf{s}$ only):

$$\mathcal{L}_{\hat{\mathbf{s}}_{i\rightarrow j}} = \frac{1}{|\mathcal{R}||\mathcal{N}|} \sum_{\mathbf{r}_i \in \mathcal{R}} \sum_{j \in \mathcal{N}} \hat{w}_{i\rightarrow j}(\mathbf{r}_i) ||\hat{\mathbf{s}}_{i\rightarrow j}(\mathbf{r}_i) - \hat{\mathbf{s}}_j^{\dagger}(\mathbf{r}_j)||_2^2 \quad (14)$$

Finally, as supervision, we add respective losses on the reconstruction of the 2D semantic and attention features from projected 3D volume points (showing $\mathbf{s}$ only):

$$\mathcal{L}_{\hat{\mathbf{s}}} = \frac{1}{|\mathcal{R}|} \sum_{\mathbf{r}_i \in \mathcal{R}} ||\hat{\mathbf{s}}_i(\mathbf{r}_i) - \hat{\mathbf{s}}_i^{\dagger}(\mathbf{r}_i)||_2^2 \quad (15)$$

Unlike depth and scene flow priors, these are not priors—there is no self-consistency for semantics to constrain their values. Thus, we *do not* decay their contribution. While decaying avoids disagreements between semantic and attention features and color-enforced scene geometry, it also leads to a loss of useful meaning (please see supplemental).

Thus our final loss becomes:

$$\mathcal{L}_{\text{SAFF}} = \mathcal{L}_{\hat{\mathbf{c}}} + \lambda_{\hat{\mathbf{c}}_{i\rightarrow j}} \mathcal{L}_{\hat{\mathbf{c}}_{i\rightarrow j}} + \lambda_{\hat{d}} \mathcal{L}_{\hat{d}} + \lambda_{\hat{\mathbf{p}}} \mathcal{L}_{\hat{\mathbf{p}}} \quad (16)$$
$$+ \lambda_{\hat{\mathbf{s}}_{i\rightarrow j}} \mathcal{L}_{\hat{\mathbf{s}}_{i\rightarrow j}} + \lambda_{\hat{\mathbf{a}}_{i\rightarrow j}} \mathcal{L}_{\hat{\mathbf{a}}_{i\rightarrow j}} + \lambda_{\hat{\mathbf{s}}} \mathcal{L}_{\hat{\mathbf{s}}} + \lambda_{\hat{\mathbf{a}}} \mathcal{L}_{\hat{\mathbf{a}}}$$

3.3. Semantic Attention Pyramids

When thinking about scenes, we might argue that semantics from an ideal extractor should be scale invariant, as distant objects have the same class as close objects. We might also argue that saliency (or attention features) may not be scale invariant, as small details in a scene should only be salient when viewed close up. In practice, both extracted features vary across scale and have limited resolution, e.g., DINO-ViT [6] produces one output for each 8×8 patch. But, from this, we want semantic features and saliency for every RGB pixel that still respects scene boundaries.

Thus far, work on *static* scenes has ignored the input/feature resolution mismatch [18] as multi-view constraints provide improved localization within the volume. For monocular video, this approach has limitations [43]. Forming many constraints on dynamic objects requires long-term motion correspondence—a tricky task—and so we want to maximize the resolution of any input features where possible without changing their meaning.

One way may be through a pyramid of semantic and attention features that uses a sliding window approach at finer resolutions. Averaging features could increase detail around edges, but we must overcome the practical limit that these features are not stable across scales. This is especially important for saliency: unlike typical RGB pyramids that must preserve energy in an alias-free way [2], saliency changes significantly over scales and does not preserve energy.

Consider a feature pyramid $\mathcal{P}$ with loss weights per level:

$$\mathcal{L}_{\mathcal{P}\hat{\mathbf{s}}} = \sum_{i \in \mathcal{P}} \lambda_{\hat{\mathbf{s}}}^i \mathcal{L}_{\hat{\mathbf{s}}}^i \qquad \mathcal{L}_{\mathcal{P}\hat{\mathbf{a}}} = \sum_{i \in \mathcal{P}} \lambda_{\hat{\mathbf{a}}}^i \mathcal{L}_{\hat{\mathbf{a}}}^i \quad (17)$$

Naively encouraging scale-consistent semantics and whole-image saliency, e.g., $\lambda_{\hat{\mathbf{s}}} = \{1/3, 1/3, 1/3\}$ with $\lambda_{\hat{\mathbf{a}}} = \{1, 0, 0\}$, empirically leads to poor recovered object edges because the balanced semantics and coarse saliency compete over where the underlying geometry is. Instead, we weight both equally $\lambda_{\hat{\mathbf{s}}} = \lambda_{\hat{\mathbf{a}}} = \{1/9, 4/9, 4/9\}$. Even though the coarse layer has smaller weight, it is sufficient to guide the overall result. This balances high resolution edges from fine layers and whole object features from coarse layers while reducing geometry conflicts, and leads to improved features (Fig. 3).

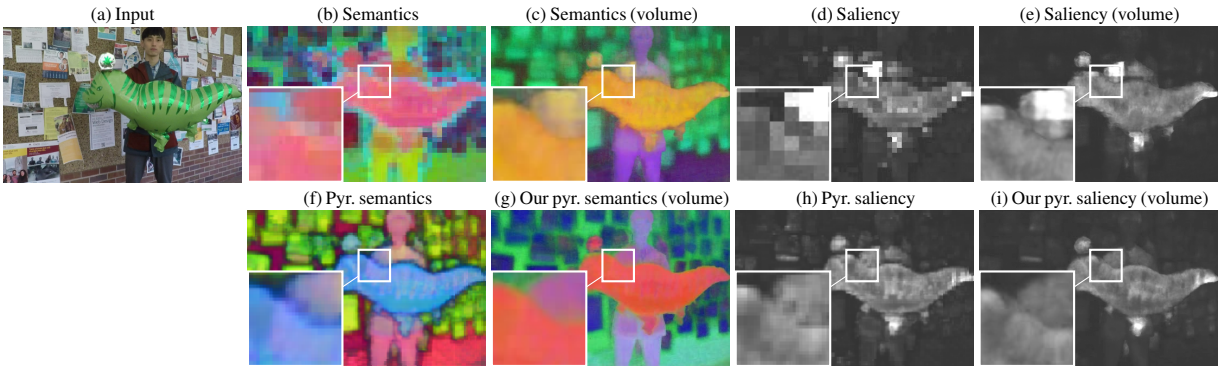

Figure 3: **Semantics and saliency improve by both volume integration and by our pyramid.** On *Balloon NBoard*, blocky artifacts are removed. Semantics are visualized as most significant three PCA dimensions; specific colors are less meaningful.

Of course, any sliding window must contain an object to extract reliable features for that object. At coarse levels, an object is always in view. At fine levels, an object is only captured in *some* windows. Objects of interest tend to be near the middle of the frame, meaning that boundary windows at finer pyramid levels contain features that less reliably capture those objects. This can cause spurious connections in clustering. To cope with this, we relatively decrease finer level boundary window weights: We upsample all levels to the finest level, then increase the coarsest level weight towards the frame boundary to $\lambda_{\hat{\mathbf{s}}} = \lambda_{\hat{\mathbf{a}}} = \{1/3, 1/3, 1/3\}$.

3.4. Using SAFF for Saliency-aware Clustering

We now wish to isolate salient objects. Even in dynamic scenes, relevant objects may not move, so analyzing dynamic elements is insufficient (cf. [47]). One approach predicts segmentation end-to-end [24]. However, end-to-end learning requires priors about the scene provided by supervision, and even large-scale pretraining might fail given unseen test scenes. To achieve scene-specific decompositions from per-video semantics, inspired by Amir *et al*. [1], we design clustering for spacetime volumes that allows segmenting novel spatio-temporal views. While DINO-ViT is trained on images, its features are loosely temporally consistent [6].

Some works optimize a representation with a fixed number of clusters, e.g., via slot attention [25] in NeRFs [39, 52]. Instead, we cluster using elbow k-means, letting us adaptively find the number of clusters after optimization. This is more flexible than baking an anticipated number of slots (sometimes with fixed semantics), and lets us cluster and segment in novel spatio-temporal viewpoints.

We demonstrate clustering results in both 3D over time and on rendered volume 2D projections over time. Given the volume reconstruction, we might think that clustering directly in 3D would be better. But, monocular input with narrow baselines makes it challenging to precisely reconstruct geometries: Consider that depth integrated a long a ray can still be accurate even though geometry at specific 3D points may be inaccurate or 'fluffy'. As such, we use the 2D volume projection clustering results in 2D comparisons.

Method For 3D over time, we sample points from the SAFF uniformly along input rays ($128\times H\times W$) and treat each pixel as a feature point, e.g., semantics are 64 dim. and saliency is 1 dim. For volume projection, we render to N input poses ($N\times H\times W$), and treat each pixel as a feature point instead. In either case, we cluster all feature points together using elbow k-means to produce an initial set of separate regions. For each cluster c, for each image, we calculate the mean attention of all feature points within the cluster $\bar{\mathbf{a}}_c$. If $\bar{\mathbf{a}}_c > 0.07$, then this cluster is salient for this image. Finally, all feature points vote on saliency: if more than 70% agree, the cluster is salient.

Salient objects may still be split into semantic parts: *e.g*., in Fig. 4, the person's head/body are separated. Plus, unwanted background saliency may exist, *e.g*., input $\hat{\mathbf{a}}^{\dagger}$ is high for the teal graphic on the wall. As such, before saliency voting, we merge clusters whose centroids have a cosine similarity > 0.5. This reduces the first problem as heads and bodies are similar, and reduces the second problem as merging the graphic cluster into the background reduces its *average* saliency (Fig. 4).

To extract an object from the 3D volume, we sample 3D points along each input ray, then ascribe the label from the semantically-closest centroid. All clusters not similar to the stored salient clusters are marked as background with zero density. For novel space-time views, we render feature images from the volume, then assign cluster labels to each pixel according to its similarity with stored input view centroids.

4. Experiments

We show the impact of adding semantic and saliency features through scene decomposition and foreground experiments. Our website contains supplemental videos.

Data: NVIDIA Dynamic Scene Dataset (Masked) This data [51] has 8 sequences of 24 time steps formed from 12 cameras simultaneously capturing video. We manually anno-

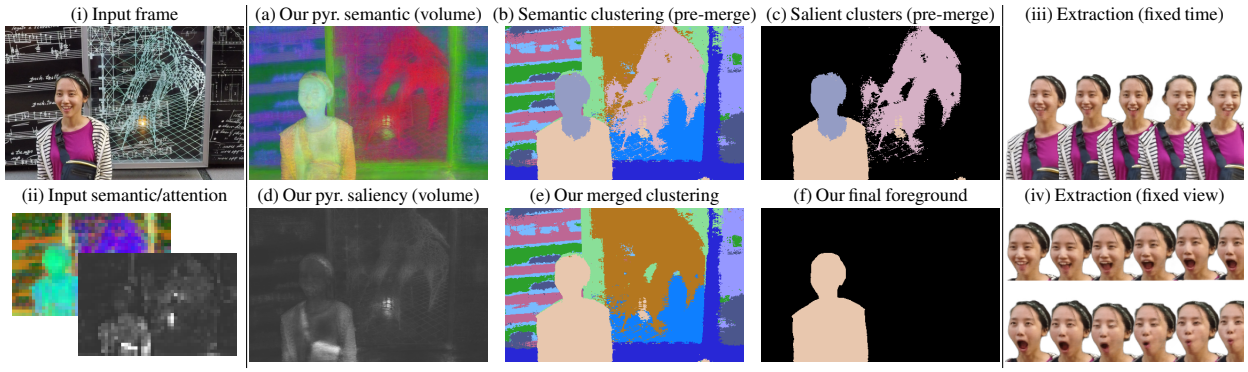

Figure 4: **Saliency-aware clustering improves decomposition.** On *Dynamic Face*, the head and body are semantically and saliently different, but are mutually different from the background. This allows us to extract a time-varying 3D field of the object.

tate object masks for view and time step splits; we will release this data publicly. We define three data splits per sequence:

1. *Input*: A monocular camera that moves position for every timestep is simulated from the input sequences; we use Yoon *et al.*'s input sequences [51].
2. *Fix Cam 0* (hold out): We fix the camera at position 0 as time plays, requiring novel view and time synthesis. $\{(\text{cam}_0, \text{time}_i), i \in [1, 2, ...23]\}$.
3. *Fix Time 0* (hold out): We fix time at step 0 as the camera moves, requiring novel view and time synthesis. $\{(\text{cam}_i, \text{time}_0), i \in [1, 2, ...11]\}$.

Data: DyCheck Dataset (Masked) For single-camera casual monocular data, we select a subset of Gao et al.'s DyCheck dataset [11]. We remove scenes without an obvious subject, e.g., where telling foreground from background is hard even for a human. We select *haru-sit*, *space-out*, *spin*, *paper-windmill*, and *mochi-high-five*. We uniformly sample 48 frames and manually annotate object masks. We take even frames as the input set and odd frames as the hold out set. We use the same hyperparameters between both datasets.

Metrics To assess clustering performance, we use the Adjusted Rand Index (ARI; $[-1, 1]$). This compares the similarity of two assignments without label matching, where random assignment would score $\approx$0. For foreground segmentation, we compute IoU (Jaccard), and for RGB quality we use PSNR, SSIM, and LPIPS.

4.1. Comparisons including ablations

SAFF (ours) We optimize upon the input split of each scene, and perform clustering to obtain object segmentations. To produce a foreground, we merge all salient objects.

SAFF (3D) The same as above, but processed in 3D rather than on 2D volume projections.

— w/ pyr $\lambda_{\hat{\mathbf{a}}} = \{1, 0, 0\}$ Pyramid with only coarse saliency (Sec. 3.3) and balanced semantic weight across levels.

— w/o pyr No pyramid (Sec. 3.3); we optimize with features and saliency extracted from the input image only.

— w/o merge With pyramid, but we remove cluster merging inside the saliency-aware clustering algorithm.

— w/ blend v To compare generic dynamic segmentation to saliency segmentation, we use the static/dynamic weight instead of volume saliency to segment foreground objects. We set every pixel below the 80% v quantile in each image to be background, or otherwise foreground.

— w/ post process We add a step after the saliency-aware clustering to refine edges using a conditional random field (please see supplemental material for details). This gains significantly from the depth estimated via volume reconstruction, producing sharp and detailed edges.

NSFF [22] This method cannot produce semantic clusterings. While saliency and blend weight v have different meanings, if we compare our v to NSFF's, then we can see any impact of a shared backbone with attention heads upon the static/dynamic separation. We disable the supervised motion mask initialization in NSFF as our method does not use such information.

D^{2}NeRF [47] This method also cannot produce semantic clusterings. Over HyperNeRF [33], it adds a shadow field network and further losses to try to isolate objects into the dynamic NeRF over the separate static one. The paper also compares to NSFF without motion mask initialization.

DINO-ViT (2D) [1] We ignore the volume and pass 2D semantic and attention features into the clustering algorithm. This cannot apply to novel viewpoints. Instead, we evaluate the approach upon *all* multi-view color images—input and hold-out—whereas other methods must render hold-out views. With our added pyramid processing (Sec. 3.3).

— w/o pyr No pyramid; upsample to input RGB size.

ProposeReduce (2D) [24] As a general comparison point, we apply this state-of-the-art 2D video segmentation method. For object segmentation, we use a ProposeReduce network

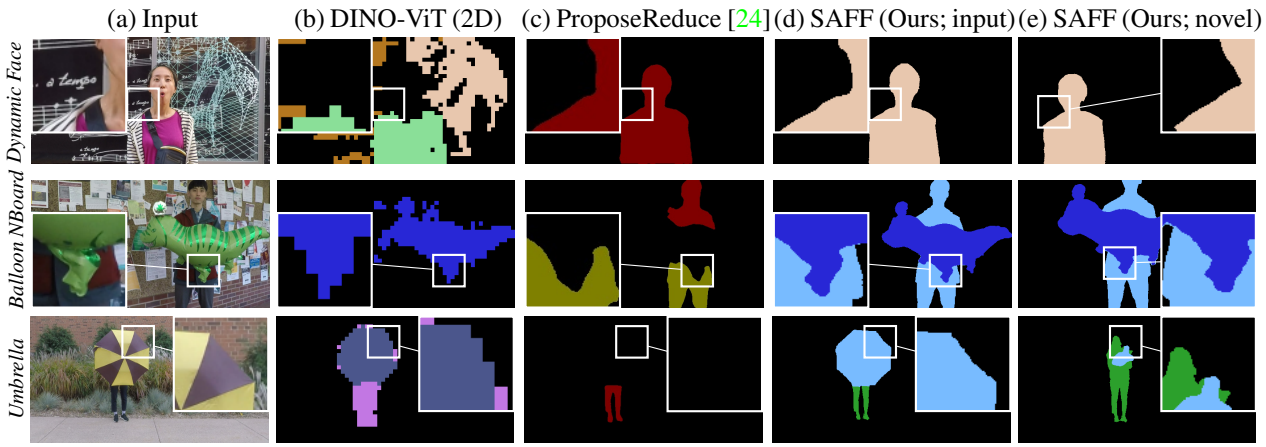

Figure 5: **SAFF object segmentations show balanced quality while recovering a volumetric scene representation (e).** Basic DINO-ViT produces low-quality segmentations and misses objects. A state-of-the-art 2D video learning method [24] sometimes has edge detail (*Umbrella*, legs) but othertimes misses detail and objects (*Balloon NBoard*).

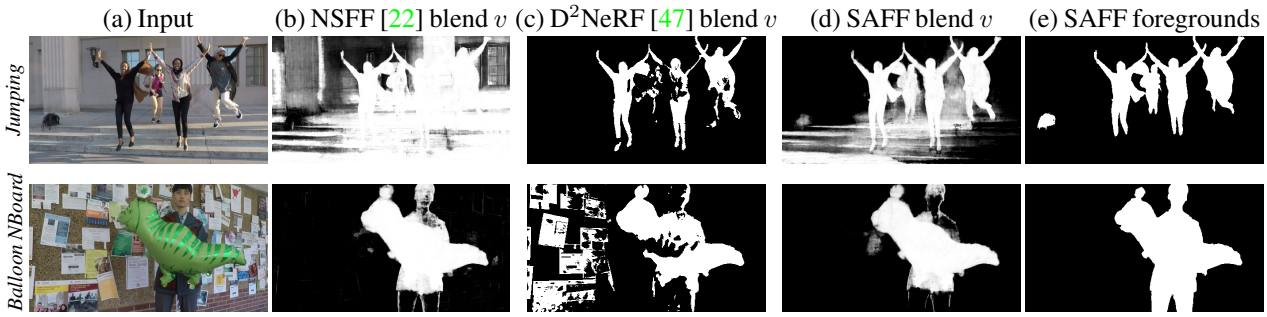

Figure 6: **Saliency improves foreground segmentation.** Static/dynamic separations are not foreground segmentations, leading to limited use of dynamic NeRF models for downstream tasks. Minor improvements to dynamic blending weight v are seen in some sequences (*Jumping*) by adding the saliency head to the shared backbone.

that was pretrained with supervision on YouTube-VIS 2019 [49] for instance segmentation. For foreground segmentation, we use weights pretrained on UVOS [5] intended specifically for unsupervised foreground segmentation. As ProposeReduce is only a 2D method, we provide it with hold-out images for splits with novel views rather than our approach that must render novel views at hold-out poses.

4.2. Findings

Dynamic scene decomposition We separate the background and each foreground object individually (Tab. 1). The baseline 2D DINO-ViT method is improved by our pyramid approach. But, being only 2D, this fails to produce a consistent decomposition across novel spacetime views even when given ground truth hold-out images. This shows the value of a volume integration. Next, supervised ProposeReduce produces good results (Fig. 5), but sometimes misses salient objects or fails to join them behind occluding objects, and only sometimes produces better edges than our method without post-processing as it can oversmooth edges. ProposeReduce also receives ground truth images in hold-out sets.

Instead, our approach must render hold-out views via the volume reconstruction. This produces more consistent segmentations through spacetime manipulations—this is the added value of volume integration through learned saliency and attention heads. Ablated components show the value of our pyramid step, its coarse-saliency-only variant, and the cluster merge and image post processing steps. Qualitatively, we see good detail (Fig. 5); post-processing additionally improves edge quality and removes small unwanted regions.

Oracle saliency We also include an oracle experiment where saliency voting is replaced by cluster selection based on ground truth masks. This experiment tells us what part of the performance gap lies with saliency itself, and what remains due to volume integration and cluster boundary issues. With oracle clusters, our decomposition performance is 0.8 ARI (Tab. 1) even in hold-out views. This shows that our existing cluster boundaries are accurate, and that accurate saliency for object selection is the larger remaining problem.

Foreground segmentation We simplify the problem and consider all objects as simply 'foreground' to compare to methods that do not produce per object masks. Here,

Table 1: **Spacetime volume integration improves dynamic scene decomposition.** Pyramid construction and cluster merging help quantitatively, and ours is comparable to SOTA supervised 2D video segmentation network ProposeReduce. Metric: Adjusted Rand Index ($[-1, 1]$, higher is better).

	Input	Fix Cam 0	Fix Time 0
ProposeReduce (2D)	0.725	0.736	0.742
DINO-ViT (2D)	0.501	0.495	0.321
w/o pyr $\hat{\mathbf{s}}, \hat{\mathbf{a}}$	0.470	0.464	0.346
SAFF (3D)	0.594	0.578	0.566
SAFF (ours)	0.653	0.634	0.625
w/ pyr $\lambda_{\hat{\mathbf{a}}} = \{1, 0, 0\}$	0.620	0.598	0.592
w/o pyr $\hat{\mathbf{s}}, \hat{\mathbf{a}}$	0.545	0.532	0.521
w/o merge cluster	0.593	0.574	0.563
w/ post process	0.759	0.733	0.735
w/ oracle	0.834	0.806	0.800
w/ oracle + post process	0.922	0.890	0.880

Table 2: **Saliency improves foreground segmentation.** Adding saliency also slightly aids how much static/dynamic blend weight v represents the foreground (cf. NSFF blend v to SAFF's). Here, ProposeReduce uses unsupervised training and data [5]. Metric: IoU/Jaccard ($[0, 1]$, higher is better).

	Input	Fix Cam 0	Fix Time 0
ProposeReduce (2D)	0.609	0.464	0.591
DINO-ViT (2D)	0.381	0.382	0.357
NSFF — blend v	0.322	0.309	0.268
D^{2}NeRF— blend v	0.470	0.334	0.269
SAFF — saliency	0.609	0.589	0.572
— blend v	0.388	0.380	0.329
— post process v	0.720	0.694	0.679

Table 3: **SAFF semantics generalize to DyCheck Dataset (Masked)** Oracle saliency. ProposeReduce is given ground truth test frames, while SAFF must render them. SAFF is comparable to SOTA supervised 2D video segmentation network ProposeReduce. Metric: Adjusted Rand Index ($[-1, 1]$, higher is better); IoU/Jaccard index ($[-1, 1]$, higher is better).

	ARI		IoU	
	Input	Test	Input	Test
ProposeReduce (2D)	0.761	0.762	0.761	0.762
DINO-ViT (2D)	0.801	0.800	0.797	0.797
SAFF (3D)	0.902	0.820	0.910	0.812

the same trend continues (Tab. 2). We note more subtle improvements to static/dynamic blending weights when adding our additional feature heads to the backbone MLP, and overall show that adding top-down information helps produce more useful object masks. Qualitative results show whole objects in the foreground rather than broad regions of possible dynamics (NSFF) or broken objects (D^{2}NeRF; Fig. 6).

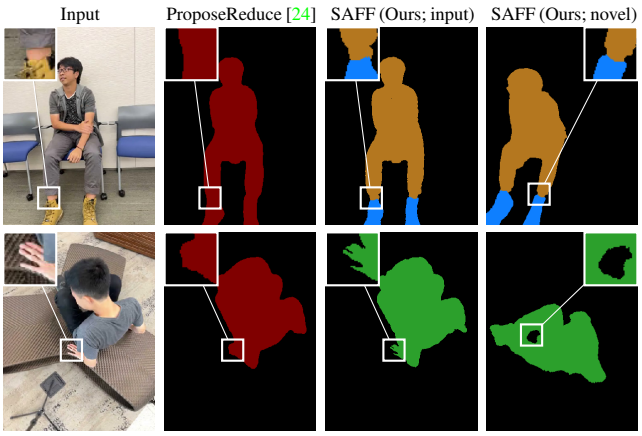

Figure 7: **SAFF can apply to DyCheck Dataset (Masked).** SAFF is comparable to supervised large-scale 2D video learning [24]. Some fine details are improved (bottom, fingers) and novel views maintain their geometry (bottom, gap between legs occluded by head at input timestep).

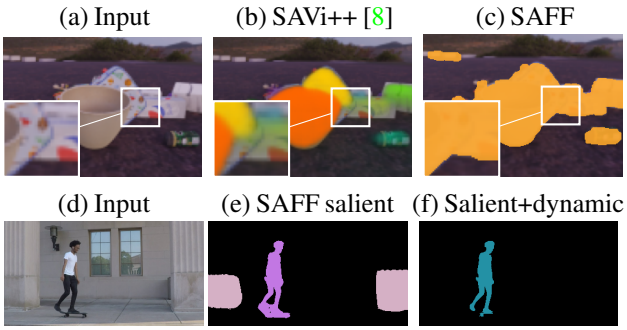

Figure 8: **Limitations.** DINO-ViT is not instance-aware, causing unwanted grouping (c). Unwanted static objects may be salient; assuming salient objects are dynamic fixes this (f).

DyCheck evaluation DyCheck often has close-up objects and, even with our selected sequences, saliency struggles to find foreground objects. Thus, we use oracle saliency. DINO-ViT and ProposeReduce are given test views while SAFF must render them. Quantitative (Tab. 3) and qualitative (Fig. 7) experiments show similar trends as before: ProposeReduce is good but may miss objects and fine details; SAFF may produce finer details and is more geometrically consistent.

5. Discussion and Limitations

DINO-ViT features are not instance-aware (Fig. 8). This is in contrast to object-centric learning approaches that aim to identify individual objects. To represent these different approaches, we compare to a result from slot-attention based SAVi++ [8]. This method trains on thousands of supervised MOVi [12] sequences with per-object masks, whereas we use generic pre-trained features and gain better edges from volume integration. Combining these two approaches could give accurate instance-level scene objects.

DINO-ViT saliency may attend to unwanted regions. In

Figure 8d–e, the static pillars could be isolated using scene flow. But, often our desired subjects do not move (cf. people in *Umbrella* or *Balloon NBoard*). For tasks or data that can assume that salient objects are dynamic, we use SAFF's 4D scene reconstruction to reject static-but-salient objects by merging clusters via scene flow: First, we project $\mathbf{f}$ over each timestep into each input camera pose—this simulates optical flow with a static camera. Clusters are marked as salient per image if mean flow magnitude per cluster $|\bar{\mathbf{p}}| > 0.07$ *and* mean attention $\bar{\mathbf{a}}_c > 0.07$. Finally, as before, a cluster is globally salient if 70% of images agree (Fig. 8f).

Acknowledgements The CV community in New England for feedback, and funding from NSF CNS-2038897 and an Amazon Research Award. Eliot thanks a Randy F. Pausch '82 Undergraduate Summer Research Award at Brown CS.

References

[1] Shir Amir, Yossi Gandelsman, Shai Bagon, and Tali Dekel. Deep vit features as dense visual descriptors. *arXiv preprint arXiv:2112.05814*, 2021. 2, 4, 5, 6, 20

[2] Jonathan T Barron, Ben Mildenhall, Matthew Tancik, Peter Hedman, Ricardo Martin-Brualla, and Pratul P Srinivasan. Mip-nerf: A multiscale representation for anti-aliasing neural radiance fields. In *Proceedings of the IEEE/CVF International Conference on Computer Vision*, pages 5855–5864, 2021. 4

[3] Kenneth Blomqvist, Lionel Ott, Jen Jen Chung, and Roland Y. Siegwart. Baking in the feature: Accelerating volumetric segmentation by rendering feature maps. *ArXiv*, abs/2209.12744, 2022. 2

[4] Christopher P. Burgess, Loïc Matthey, Nicholas Watters, Rishabh Kabra, Irina Higgins, Matthew M. Botvinick, and Alexander Lerchner. Monet: Unsupervised scene decomposition and representation. *ArXiv*, abs/1901.11390, 2019. 1, 2, 12

[5] Sergi Caelles, Jordi Pont-Tuset, Federico Perazzi, Alberto Montes, Kevis-Kokitsi Maninis, and Luc Van Gool. The 2019 davis challenge on vos: Unsupervised multi-object segmentation. *arXiv:1905.00737*, 2019. 2, 7, 8, 13

[6] Mathilde Caron, Hugo Touvron, Ishan Misra, Hervé Jégou, Julien Mairal, Piotr Bojanowski, and Armand Joulin. Emerging properties in self-supervised vision transformers. In *Proceedings of the International Conference on Computer Vision (ICCV)*, 2021. 1, 2, 4, 5

[7] Anpei Chen, Zexiang Xu, Andreas Geiger, Jingyi Yu, and Hao Su. Tensorf: Tensorial radiance fields. *arXiv preprint arXiv:2203.09517*, 2022. 20

[8] Gamaleldin F. Elsayed, Aravindh Mahendran, Sjoerd van Steenkiste, Klaus Greff, Michael C. Mozer, and Thomas Kipf. SAVi++: Towards end-to-end object-centric learning from real-world videos. In *Advances in Neural Information Processing Systems*, 2022. 1, 2, 8, 12

[9] Zhiwen Fan, Peihao Wang, Yifan Jiang, Xinyu Gong, Dejia Xu, and Zhangyang Wang. Nerf-sos: Any-view self-supervised object segmentation on complex scenes. *ArXiv*, abs/2209.08776, 2022. 2

[10] Xiao Fu, Shangzhan Zhang, Tianrun Chen, Yichong Lu, Lanyun Zhu, Xiaowei Zhou, Andreas Geiger, and Yiyi Liao. Panoptic nerf: 3d-to-2d label transfer for panoptic urban scene segmentation. In *International Conference on 3D Vision (3DV)*, 2022. 2

[11] Hang Gao, Ruilong Li, Shubham Tulsiani, Bryan Russell, and Angjoo Kanazawa. Monocular dynamic view synthesis: A reality check. In *NeurIPS*, 2022. 1, 6, 13, 14

[12] Klaus Greff, Francois Belletti, Lucas Beyer, Carl Doersch, Yilun Du, Daniel Duckworth, David J. Fleet, Dan Gnanapragasam, Florian Golemo, Charles Herrmann, Thomas Kipf, Abhijit Kundu, Dmitry Lagun, Issam H. Laradji, Hsueh-Ti Liu, Henning Meyer, Yishu Miao, Derek Nowrouzezahrai, Cengiz Oztireli, Etienne Pot, Noha Radwan, Daniel Rebain, Sara Sabour, Mehdi S. M. Sajjadi, Matan Sela, Vincent Sitzmann, Austin Stone, Deqing Sun, Suhani Vora, Ziyu Wang, Tianhao Wu, Kwang Moo Yi, Fangcheng Zhong, and Andrea Tagliasacchi. Kubric: A scalable dataset generator. *2022 IEEE/CVF Conference on Computer Vision and Pattern Recognition (CVPR)*, pages 3739–3751, 2022. 8

[13] Klaus Greff, Raphael Lopez Kaufman, Rishabh Kabra, Nicholas Watters, Christopher P. Burgess, Daniel Zoran, Loïc Matthey, Matthew M. Botvinick, and Alexander Lerchner. Multi-object representation learning with iterative variational inference. In *ICML*, 2019. 2, 12

[14] Basile Van Hoorick, Purva Tendulka, Dídac Surís, Dennis Park, Simon Stent, and Carl Vondrick. Revealing occlusions with 4d neural fields. *2022 IEEE/CVF Conference on Computer Vision and Pattern Recognition (CVPR)*, pages 3001–3011, 2022. 2

[15] Jeff Johnson, Matthijs Douze, and Hervé Jégou. Billion-scale similarity search with GPUs. *IEEE Transactions on Big Data*, 7(3):535–547, 2019. 20

[16] Rishabh Kabra, Daniel Zoran, Goker Erdogan, Loïc Matthey, Antonia Creswell, Matthew M. Botvinick, Alexander Lerchner, and Christopher P. Burgess. Simone: View-invariant, temporally-abstracted object representations via unsupervised video decomposition. *ArXiv*, abs/2106.03849, 2021. 1, 2, 12

[17] Thomas Kipf, Gamaleldin F. Elsayed, Aravindh Mahendran, Austin Stone, Sara Sabour, Georg Heigold, Rico Jonschkowski, Alexey Dosovitskiy, and Klaus Greff. Conditional Object-Centric Learning from Video. In *International Conference on Learning Representations (ICLR)*, 2022. 1, 2, 12

[18] Sosuke Kobayashi, Eiichi Matsumoto, and Vincent Sitzmann. Decomposing nerf for editing via feature field distillation. In *Advances in Neural Information Processing Systems*, volume 35, 2022. 1, 2, 4, 12, 20

[19] Johannes Kopf, Xuejian Rong, and Jia-Bin Huang. Robust consistent video depth estimation. In *Proceedings of the IEEE/CVF Conference on Computer Vision and Pattern Recognition*, pages 1611–1621, 2021. 13

[20] Philipp Krähenbühl and Vladlen Koltun. Efficient inference in fully connected crfs with gaussian edge potentials. In J. Shawe-Taylor, R. Zemel, P. Bartlett, F. Pereira, and K.Q. Weinberger, editors, *Advances in Neural Information Processing Systems*, volume 24. Curran Associates, Inc., 2011. 20

[21] Abhijit Kundu, Kyle Genova, Xiaoqi Yin, Alireza Fathi, Caroline Pantofaru, Leonidas J. Guibas, Andrea Tagliasacchi, Frank Dellaert, and Thomas Funkhouser. Panoptic neural fields: A semantic object-aware neural scene representation.

In *Proceedings of the IEEE/CVF Conference on Computer Vision and Pattern Recognition (CVPR)*, pages 12871–12881, June 2022. 2, 12

[22] Zhengqi Li, Simon Niklaus, Noah Snavely, and Oliver Wang. Neural scene flow fields for space-time view synthesis of dynamic scenes. In *Proceedings of the IEEE/CVF Conference on Computer Vision and Pattern Recognition (CVPR)*, 2021. 1, 2, 6, 7, 12, 14, 15, 20, 21

[23] Chen-Hsuan Lin, Wei-Chiu Ma, Antonio Torralba, and Simon Lucey. Barf: Bundle-adjusting neural radiance fields. In *Proceedings of the IEEE/CVF International Conference on Computer Vision*, pages 5741–5751, 2021. 13

[24] Huaijia Lin, Ruizheng Wu, Shu Liu, Jiangbo Lu, and Jiaya Jia. Video instance segmentation with a propose-reduce paradigm. *2021 IEEE/CVF International Conference on Computer Vision (ICCV)*, pages 1719–1728, 2021. 1, 5, 6, 7, 8, 12

[25] Francesco Locatello, Dirk Weissenborn, Thomas Unterthiner, Aravindh Mahendran, Georg Heigold, Jakob Uszkoreit, Alexey Dosovitskiy, and Thomas Kipf. Object-centric learning with slot attention. *arXiv preprint arXiv:2006.15055*, 2020. 1, 2, 5, 12

[26] Kirill Mazur, Edgar Sucar, and Andrew J. Davison. Feature-realistic neural fusion for real-time, open set scene understanding. *ArXiv*, abs/2210.03043, 2022. 2

[27] Luke Melas-Kyriazi, Christian Rupprecht, Iro Laina, and Andrea Vedaldi. Deep spectral methods: A surprisingly strong baseline for unsupervised semantic segmentation and localization. In *CVPR*, 2022. 2

[28] Ben Mildenhall, Pratul P. Srinivasan, Matthew Tancik, Jonathan T. Barron, Ravi Ramamoorthi, and Ren Ng. Nerf: Representing scenes as neural radiance fields for view synthesis. In *ECCV*, 2020. 2, 3

[29] Tom Monnier, Elliot Vincent, Jean Ponce, and Mathieu Aubry. Unsupervised layered image decomposition into object prototypes. In *Proceedings of the IEEE/CVF International Conference on Computer Vision (ICCV)*, pages 8640–8650, October 2021. 2

[30] Thomas Müller, Alex Evans, Christoph Schied, and Alexander Keller. Instant neural graphics primitives with a multiresolution hash encoding. *arXiv preprint arXiv:2201.05989*, 2022. 20, 21

[31] Michael Niemeyer and Andreas Geiger. Giraffe: Representing scenes as compositional generative neural feature fields. In *Proc. IEEE Conf. on Computer Vision and Pattern Recognition (CVPR)*, 2021. 2

[32] Keunhong Park, Utkarsh Sinha, Jonathan T. Barron, Sofien Bouaziz, Dan B Goldman, Steven M. Seitz, and Ricardo Martin-Brualla. Nerfies: Deformable neural radiance fields. *ICCV*, 2021. 14

[33] Keunhong Park, Utkarsh Sinha, Peter Hedman, Jonathan T. Barron, Sofien Bouaziz, Dan B Goldman, Ricardo Martin-Brualla, and Steven M. Seitz. Hypernerf: A higher-dimensional representation for topologically varying neural radiance fields. *ACM Trans. Graph.*, 40(6), dec 2021. 1, 2, 6

[34] René Ranftl, Katrin Lasinger, David Hafner, Konrad Schindler, and Vladlen Koltun. Towards robust monocular depth estimation: Mixing datasets for zero-shot cross-dataset transfer. *IEEE Transactions on Pattern Analysis and Machine Intelligence*, 44(3), 2022. 2

[35] Johannes Lutz Schönberger and Jan-Michael Frahm. Structure-from-motion revisited. In *Conference on Computer Vision and Pattern Recognition (CVPR)*, 2016. 2, 13

[36] Maximilian Seitzer, Max Horn, Andrii Zadaianchuk, Dominik Zietlow, Tianjun Xiao, Carl-Johann Simon-Gabriel, Tong He, Zheng Zhang, Bernhard Scholkopf, Thomas Brox, and Francesco Locatello. Bridging the gap to real-world object-centric learning. *ArXiv*, abs/2209.14860, 2022. 2

[37] Gyungin Shin, Samuel Albanie, and Weidi Xie. Unsupervised salient object detection with spectral cluster voting. In *CVPRW*, 2022. 2

[38] Cameron Smith, Hong-Xing Yu, Sergey Zakharov, Frédo Durand, Joshua B. Tenenbaum, Jiajun Wu, and Vincent Sitzmann. Unsupervised discovery and composition of object light fields. *ArXiv*, abs/2205.03923, 2022. 1, 2, 12

[39] Karl Stelzner, Kristian Kersting, and Adam R. Kosiorek. Decomposing 3d scenes into objects via unsupervised volume segmentation. *ArXiv*, abs/2104.01148, 2021. 1, 2, 5, 12

[40] Pei Sun, Henrik Kretzschmar, Xerxes Dotiwalla, Aurelien Chouard, Vijaysai Patnaik, Paul Tsui, James Guo, Yin Zhou, Yuning Chai, Benjamin Caine, Vijay Vasudevan, Wei Han, Jiquan Ngiam, Hang Zhao, Aleksei Timofeev, Scott Ettinger, Maxim Krivokon, Amy Gao, Aditya Joshi, Yu Zhang, Jonathon Shlens, Zhifeng Chen, and Dragomir Anguelov. Scalability in perception for autonomous driving: Waymo open dataset. In *IEEE/CVF Conference on Computer Vision and Pattern Recognition (CVPR)*, June 2020. 2

[41] Zachary Teed and Jia Deng. Raft: Recurrent all-pairs field transforms for optical flow. In *European conference on computer vision*, pages 402–419. Springer, 2020. 2

[42] Edgar Tretschk, Ayush Tewari, Vladislav Golyanik, Michael Zollhöfer, Christoph Lassner, and Christian Theobalt. Non-rigid neural radiance fields: Reconstruction and novel view synthesis of a dynamic scene from monocular video. *2021 IEEE/CVF International Conference on Computer Vision (ICCV)*, pages 12939–12950, 2021. 1, 2

[43] Vadim Tschernezki, Iro Laina, Diane Larlus, and Andrea Vedaldi. Neural Feature Fusion Fields: 3D distillation of self-supervised 2D image representations. In *Proceedings of the International Conference on 3D Vision (3DV)*, 2022. 2, 4, 12

[44] Vadim Tschernezki, Diane Larlus, and Andrea Vedaldi. NeuralDiff: Segmenting 3D objects that move in egocentric videos. In *Proceedings of the International Conference on 3D Vision (3DV)*, 2021. 2

[45] Rishi Veerapaneni, John D. Co-Reyes, Michael Chang, Michael Janner, Chelsea Finn, Jiajun Wu, Joshua Tenenbaum, and Sergey Levine. Entity abstraction in visual model-based reinforcement learning. In Leslie Pack Kaelbling, Danica Kragic, and Komei Sugiura, editors, *Proceedings of the Conference on Robot Learning*, volume 100 of *Proceedings of Machine Learning Research*, pages 1439–1456. PMLR, 30 Oct–01 Nov 2020. 1

[46] Yangtao Wang, Xi Shen, Shell Xu Hu, Yuan Yuan, James L. Crowley, and Dominique Vaufreydaz. Self-supervised transformers for unsupervised object discovery using nor-

malized cut. In *Conference on Computer Vision and Pattern Recognition*, 2022. 2

[47] Tianhao Wu, Fangcheng Zhong, Andrea Tagliasacchi, Forrester Cole, and Cengiz Öztireli. D2nerf: Self-supervised decoupling of dynamic and static objects from a monocular video. *ArXiv*, abs/2205.15838, 2022. 1, 2, 5, 6, 7, 12, 15

[48] Bangbang Yang, Yinda Zhang, Yinghao Xu, Yijin Li, Han Zhou, Hujun Bao, Guofeng Zhang, and Zhaopeng Cui. Learning object-compositional neural radiance field for editable scene rendering. In *International Conference on Computer Vision (ICCV)*, October 2021. 1, 2, 12

[49] Linjie Yang, Yuchen Fan, and Ning Xu. Video instance segmentation. *2019 IEEE/CVF International Conference on Computer Vision (ICCV)*, Oct 2019. 7

[50] Vickie Ye, Zhengqi Li, Richard Tucker, Angjoo Kanazawa, and Noah Snavely. Deformable sprites for unsupervised video decomposition. In *IEEE Conference on Computer Vision and Pattern Recognition (CVPR)*, June 2022. 2

[51] Jae Shin Yoon, Kihwan Kim, Orazio Gallo, Hyun Soo Park, and Jan Kautz. Novel view synthesis of dynamic scenes with globally coherent depths from a monocular camera. In *IEEE/CVF Conference on Computer Vision and Pattern Recognition (CVPR)*, June 2020. 1, 5, 6, 13

[52] Hong-Xing Yu, Leonidas J. Guibas, and Jiajun Wu. Unsupervised discovery of object radiance fields. In *International Conference on Learning Representations*, 2022. 1, 2, 5, 12

[53] Zhoutong Zhang, Forrester Cole, Zhengqi Li, Michael Rubinstein, Noah Snavely, and William T Freeman. Structure and motion from casual videos. In *European Conference on Computer Vision*, pages 20–37. Springer, 2022. 13

[54] Shuaifeng Zhi, Tristan Laidlow, Stefan Leutenegger, and Andrew Davison. In-place scene labelling and understanding with implicit scene representation. In *Proceedings of the International Conference on Computer Vision (ICCV)*, 2021. 2

Appendix

This document contains a related work comparison table (Appendix A), details and rationale for our dataset construction (Appendix B), justification of design choices throughout the approach (Appendix D), and implementation details (Appendix E). Given the numerous figures and tables, many sections begin on a new page for easier reading.

Further, we include a supplemental website that highlights key findings and allows comparison between different methods and ablations for the different SAFF volumes. Please find it here: https://visual.cs.brown.edu/saff

A. Related Work Table

We include a table of related work (Tab. 4). This includes work in 2D image object-centric learning (IODINE [13], MONET [4], Slot Attention [25]), 2D videos (SIMONe [16], SAVi [17]), a method that considers light field input (COLF [38]), and works that add semantic information to fields (PNF [21]) including from mask supervision (Object-NeRF [48]).

Table 4: An comparison of related work in scene decomposition shows the unstudied area of real-world dynamic 3D segmentation without explicit segmentation clues. We investigate whether saliency can provide similar clues for the monocular video case. From this table, the closest related method is N3F; however, they take user input to define their segmentation.
Learning: Large-scale training data:
T: Supervised task-specific data.
P: Generic features (e.g., ImageNet).
✕: No features used.

	Dynamic (video)	Monocular	Real world	3D	No seg. clue	Learning	Adaptive # objects	Object-level
IODINE[13]	✕	✓	✕	✕	✓	✕	✕	✓
MONET[4]	✕	✓	✕	✕	✓	✕	✕	✓
Slot Attention[25]	✕	✓	✕	✕	Mask	T	✕	✓
SIMONe[16]	✓	✓	✕	✕	✓	✕	✕	✓
SAVi[17]	✓	✓	✕	✕	Mask	T	✕	✓
SAVi++[8]	✓	✓	✓	✕	Mask	T	✕	✓
ObSuRF[39]	✕	✕	✕	✓	✓	✕	✕	✓
uORF[52]	✕	✕	✕	✓	✓	✕	✕	✓
COLF[38]	✕	✕	✕	✓	✓	✕	✕	✓
PNF[21]	✓	✓	✓	✓	Mask	✕	✕	✓
Object-NeRF [48]	✕	✕	✓	✓	Mask	✕	✕	✓
DFF[18]	✕	✕	✓	✓	User	P	✓	✓
N3F[43]	✓	✓	✓	✓	User	P	✓	✓
ProposeReduce[24]	✓	✓	✓	✕	✓	T	✓	✓
NSFF[22]	✓	✓	✓	✓	Mask	✕	N/A	N/A
D^2NeRF[47]	✓	✓	✓	✓	✓	✕	N/A	N/A
SAFF (this paper)	✓	✓	✓	✓	✓	P	✓	✓

B. Dynamic Scene Dataset (Masked) Creation

To perform experiments on segmentations, we manually annotate object masks for every view and time step in the NVIDIA Dynamic Scene Dataset[51] and in the DyCheck dataset [11]. Some object masks are visualized in Fig. 9.

One natural question is why we do not use existing unsupervised video segmentation benchmarks like DAVIS [5] for evaluation. When testing these videos, we found that there is little camera motion in most of these videos. This causes classic structure-from-motion approaches like COLMAP [35] to fail to estimate camera poses, thus we cannot optimize SAFF on these sequences. Concurrent tangential work attempts to improve this situation with better pose estimation [19, 23, 53].

Further, even if we did have poses, there could be no evaluation of the sequences in a 3D sense because the scenes were only ever captured with a single camera. While collecting ground truth 3D segmentation for dynamic casual videos is difficult, as discussed in the main paper, our approach allows evaluation at novel spacetime views as the scene was initially captured with 12 cameras. This gives a sense of the ability of the method to perform consistent 3D segmentation of the dynamic scene as captured by a simulated monocular camera view (main paper, Sec, 4, paragraph 'Data').

We additionally mask five sequences within the DyCheck dataset [11]. These are captured from a single smartphone RGB camera, and so do not have large disparity from frame to frame but may have large motion. Hold-out images can be taken by not processing some images in the videos, but these require less significant interpolation ability to render novel spacetime views.

Different Data Data in different modalities like infrared or depth data are beyond the scope of our work, but better depth information through, say, time of flight imaging would be a valuable addition to monocular reconstruction.

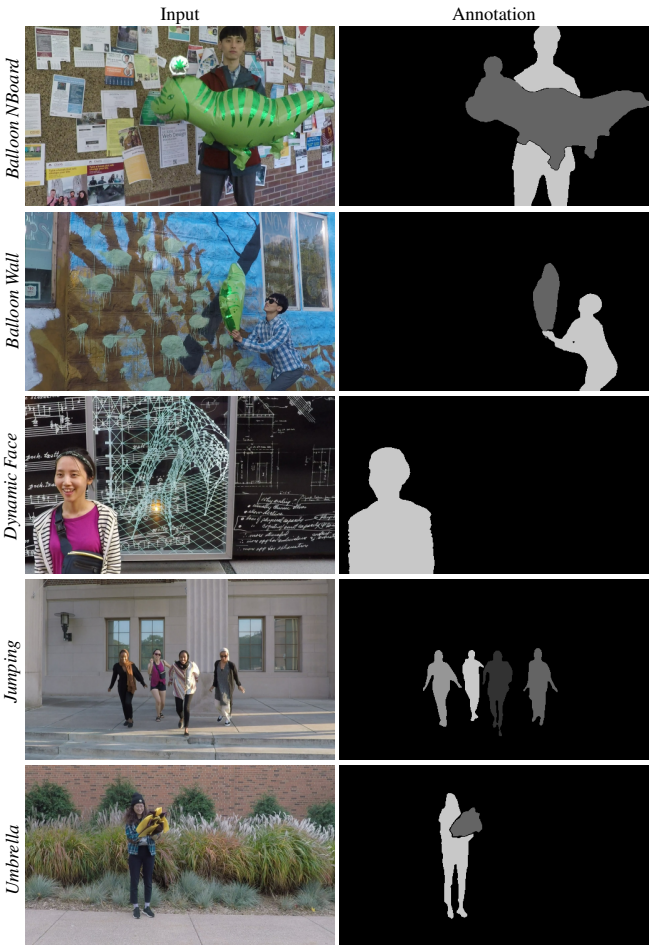

Figure 9: **Manually annotated object masks.** We store annotation masks as grayscale images. The background is assigned as pixel value 0, and foreground instances are each assigned a unique non-zero value.

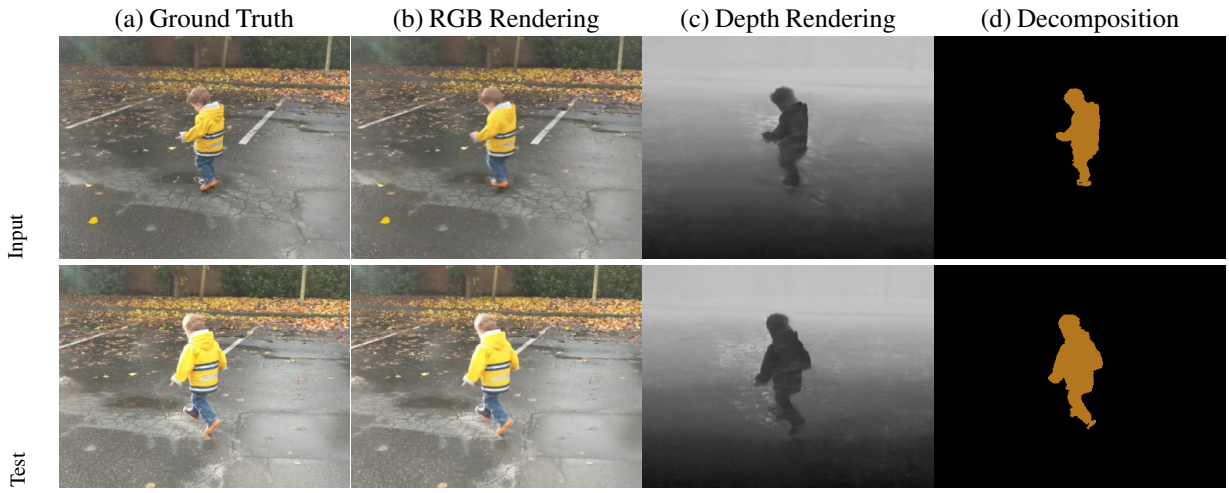

Figure 10: SAFF's rendering and decomposition result on the *kid-running* scene.

C. NSFF Extra Scene

Apart from Dynamic Scene Dataset (Masked), the NSFF [22] authors shared a *kid-running* scene to help explain their method and as a test example in their code release. Along with the smartphone sequences in DyCheck [11], this is also a 'true' monocular sequence captured with a single handheld camera. We demonstrate SAFF's decomposition result on this sequence to further demonstrate our semantic attention approach (Fig. 10).

D. Design Choices

D.1. Underlying Dynamic NeRF Approach

View synthesis and depth First, we evaluate whether RGB view synthesis performance is affected by adding more heads to the MLP. We find that it is not affected (Tab. 5). D^{2}NeRF's hyper-spacetime deformation has trouble reconstructing images on this dataset, producing distorted dynamic objects or failing to freeze time.

In Fig. 11, we show qualitatively that SAFF does not degrade view synthesis or depth quality compared to NSFF [22], while D^{2}NeRF struggles with our data.

Why does D^{2}NeRF struggle? The main distinction is that D^{2}NeRF is a deformation-based method while NSFF and SAFF are flow-based methods. For D^{2}NeRF, the scene is reconstructed in a canonical space and deformed to render the results. D^{2}NeRF struggles with larger motion in the scene—in the NVIDIA dataset, it is notably more difficult to find temporal correspondence within because frames are spatially far apart (unlike other monocular datasets created from one video camera only). Given only a monocular video to describe a scene with large camera motion *and* large object motion, it appears difficult to faithfully reconstruct both the canonical space and the deformation. In comparison, D^{2}NeRF produces good RGB reconstructions on the Nerfies [32] dataset because both the camera and scene motion are smaller than in the NVIDIA Dynamic Scene Dataset.

Table 5: **SAFF does not degrade image quality.** Adding semantics and attention on the same backbone produces the same image quality as NSFF [22]. Metrics: L is LPIPS ($[0, 1]$, lower is better), S is SSIM ($[0, 1]$, higher is better), P is PSNR ($[0, \infty]$, higher is better).

	Input			Fix Cam 0			Fix Time 0		
	L ▼	S ▲	P ▲	L	S	P	L	S	P
D^{2}NeRF	0.115	0.790	23.91	0.228	0.565	18.04	0.344	0.309	13.85
NSFF w/o masks	0.070	0.805	23.92	0.100	0.762	21.68	0.302	0.386	14.92
SAFF (ours)	0.070	0.805	23.92	0.100	0.762	21.70	0.302	0.386	14.93

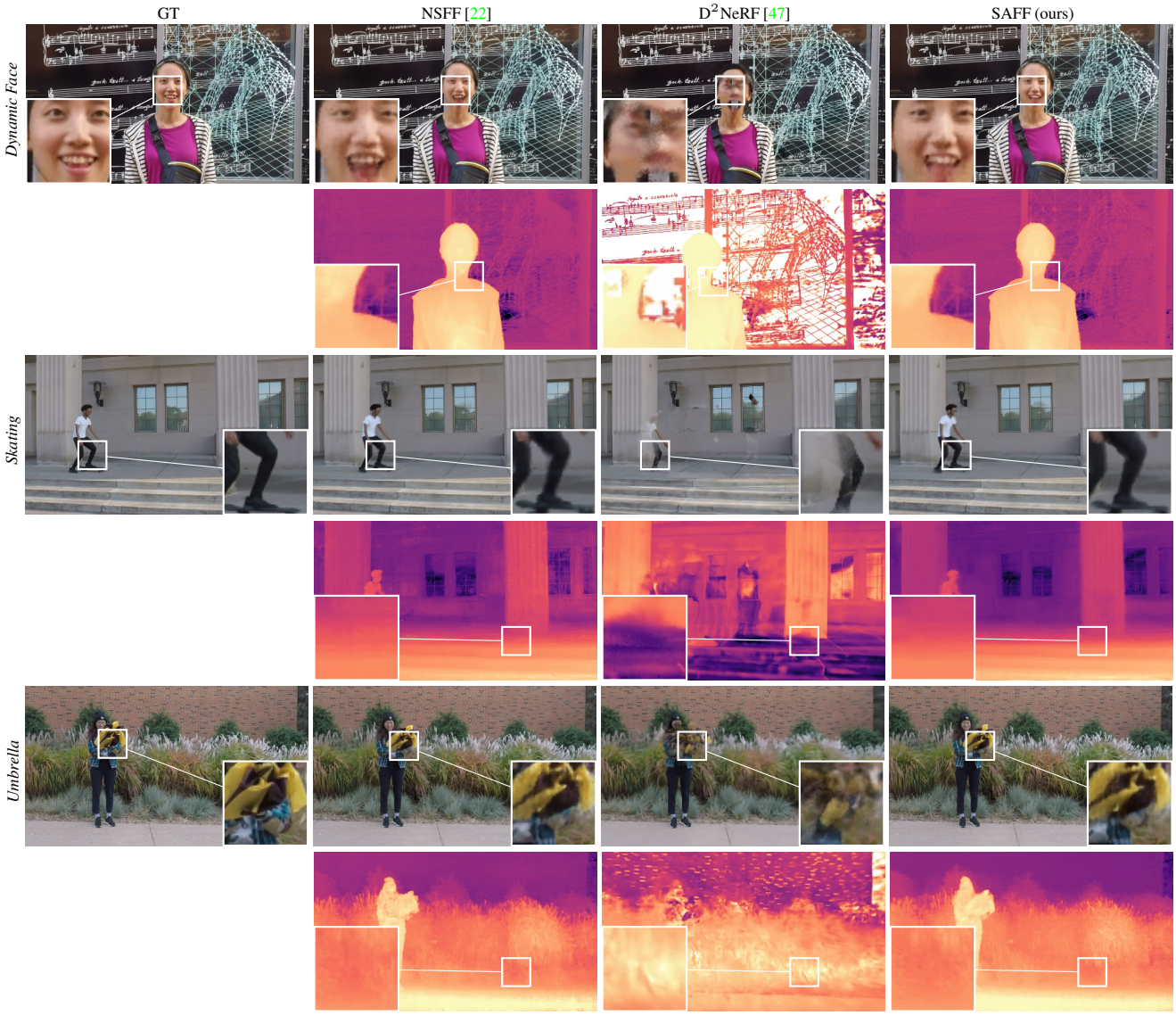

Figure 11: **SAFF does not degrade novel spacetime view synthesis or depth quality.** D^{2}NeRF struggles on the NVIDIA Dynamic Scene Dataset sequences because of the large motions between cameras.

D.2. 3D vs. 2D Projected vs. 4D Spacetime Clustering

In our saliency-aware clustering step, the elbow k-means method can take as input the per-pixel semantics features that have been sampled from 3D points in the volume (**in 3D**), or that have been rendered from the volume back to the 2D plane. Even though a volume is reconstructed, we find performance is somewhat worse when clustering in 3D than in projected 2D space (Tab. 6; and in main paper). With respect to evaluation, it is difficult to collect ground truth segmented 3D data for dynamic real world scenes (none exist to our knowledge); this remains future work.

So, why might clustering in 3D lead to worse segmentations? Given monocular input from narrow baselines and dynamic scenes, the reconstruction can be imprecise with noisy geometry. This is in contrast to dynamic scenes captured with multi-camera setups or static scenes captured with wide baselines. As semantics and saliency use the same estimated geometry as radiance, clustering in the 3D volume introduces inaccuracy in the decomposition result, thus reducing the performance quantitatively and qualitatively. We visualize the volume as a point cloud from sampled 3D points in Fig. 12. Although the volume looks natural from the training view, erroneous regions are visible when the camera pose is far away from the training view, especially on the dynamic objects.

Given direct clustering in 3D suffers from the narrow-baseline issue, we introduce another variant (**in 4D spacetime**) that also clusters upon a 3D position for each input pixel using the recovered volume density (from the estimated depth) and the timestep. While not the same as a volumetric clustering with some dense sampling, this sparse alternative is a reasonable computational compromise as our scenes contain opaque objects without participating media. We concatenate the spacetime coordinates with the semantic features for each pixel, then empirically adjust their relative weights to increase foreground segmentation performance.

In principle, this could exploit the underlying geometry to provide better edges or more instance awareness to the method. However, in practice, this does not reliably happen (Tab. 6). Any error in alignment between the semantic information and the geometry causes the clustering to confuse elements, e.g., semantics for the same object at different depths over edge boundaries. As a consequence, semantically-different entities may not be correctly separated (*Truck*), or are missing parts (*Jumping*, Fig. 13). As such, we use only projected 2D semantic features as input to the clustering.

However, even though we use semantic-attention pyramids to increase the geometric resolution of the DINO-ViT features significantly, and even though volume integration increases these still (e.g., main paper, Figure 2), one might ask whether the optimization routine could also help further align the geometry and semantic features during volume integration. This brings us to the next subsection.

Table 6: **3D volume clustering produces worse 2D segmentations than projected 2D clustering.** This is because precise localization of 3D geometry is difficult from monocular inputs for dynamic scenes. 4D spacetime clustering also produces worse foregrounds. Metric: Adjusted Rand Index ($[-1, 1]$, higher is better).

	Input	Fix Cam 0	Fix Time 0
SAFF (ours)	**0.653**	**0.634**	**0.625**
in 3D	0.594	0.578	0.566
in 4D spacetime	0.482	0.464	0.452

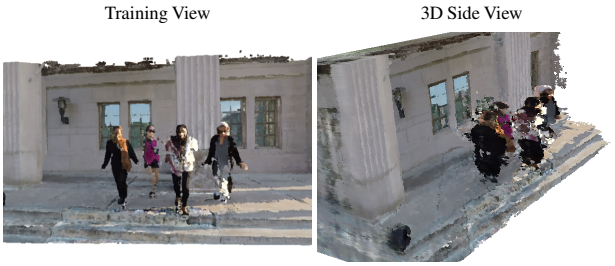

Figure 12: **3D samples.** Erroneous geometry reconstruction at regions invisible during training harms 3D clustering.

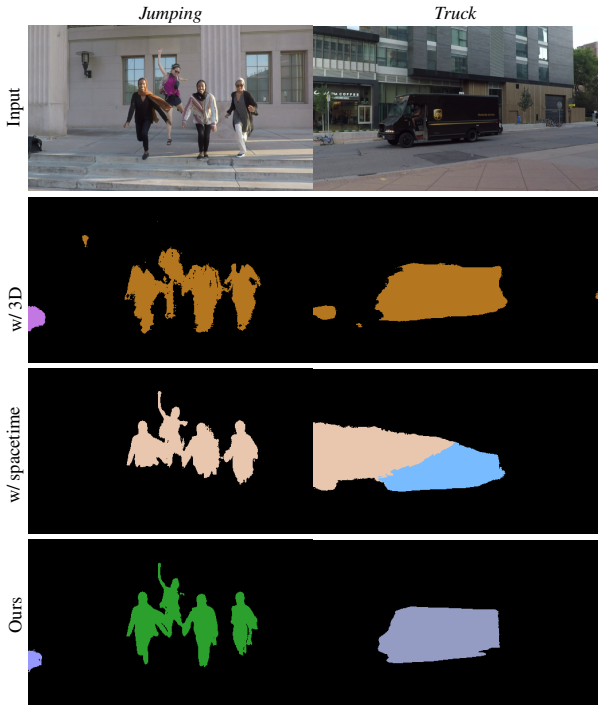

Figure 13: Clustering upon sampled 3D volume features or adding 4D spacetime features produces worse foregrounds qualitatively than just projected 2D feature clustering. This is because the narrow-baseline monocular input sometimes leads to noisy geometry estimation, and because the semantic edges must conform to the same geometry of the scene as the radiance. In 4D spacetime clustering, some clusters are confused or unnecessarily merged.

Table 7: **Decaying semantic and attention information produces overall foregrounds.** While geometric alignment improves, semantic meaning also shifts, which harms the ability of the model to correctly identify salient objects. Metric: Adjusted Rand Index ($[-1, 1]$, higher is better).

	Input	Fix Cam 0	Fix Time 0
SAFF (ours)	**0.653**	**0.634**	**0.625**
w/ decay	0.592	0.568	0.554

D.3. Decaying Semantics and Attention

One way to improve the alignment of depth edges and semantic and attention features is through decaying their reconstruction loss through training. This decay happens to the depth and optical flow priors, and for those channels of information the decay provides freedom to the optimization to refine the spacetime density once initialized with respect to the self-consistent multi-view and scene flow constraints. Intuitively, decaying the semantics and attention reconstructions would also provide more freedom to further optimize the spacetime density to minimize the self-consistent multi-view and scene flow constraints when the semantics disagreed.

However, in the main paper, we describe that semantics and attention are not priors—there is no self-consistency for semantics to constrain their values, thus, after decay the optimization is free for them to vary inconsistently and so for their reprojection to lose useful meaning. This could have unwanted consequences.

To investigate this design choice, we implement variant **w/ decay** in which we use the same decaying mechanism as depth and optical flow on $\mathcal{L}_{\hat{\mathbf{s}}}$ and $\mathcal{L}_{\hat{\mathbf{a}}}$. We also decay $\mathcal{L}_{\hat{\mathbf{s}}_{i\to j}}$ and $\mathcal{L}_{\hat{\mathbf{a}}_{i\to j}}$, because the semantics are not necessarily consistent with the spacetime geometry.

Qualitatively, adding decay does better align the semantics and attention fields with the geometry, e.g., in *Skating*, the space between skater's legs are better segmented; however, the clustering performance degrades all over the image (Fig. 14), e.g., in *Skating*, now including a sconce and unwanted floor details (zoom in). This is also reflected quantitatively (Tab. 7).

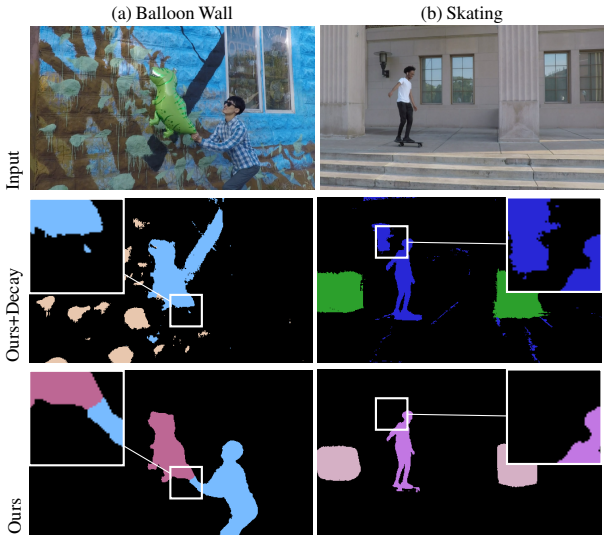

Figure 14: **Decaying semantics and attention leads to missing objects and unwanted objects.** With no self-consistent constraint, the optimization is more free to adjust the meaning of regions. While this can increase edge detail, it creates worse overall results.

D.4. Pyramid Construction

Figure 15 provides a diagrammatic example for how we construct our feature pyramids. We also provide algorithm pseudocode (Algorithm 1).

As mentioned in the main paper, given the pyramid layers, we begin conceptually from a weighted sum of three layers for semantics using $\lambda_{\hat{\mathbf{s}}} = \{1/3, 1/3, 1/3\}$ and with coarsest whole-image attention with $\lambda_{\hat{\mathbf{a}}} = \{1, 0, 0\}$. This already gives quantitatively better decomposition performance than without using a pyramid (**w/o pyr**; Tab. 8). However, the optimized semantic field does not correspond as well to scene geometry and is more influenced by error in the coarsest layer semantics and attention than our approach. For instance, the human is not identified as salient in *Balloon NBoard* (Fig. 16). Additionally, as the finer layer sliding windows do not typically contain the object of interest in boundary regions, the extracted features are incorrect. This causes unwanted clusters to appear around image edges, e.g., the gray cluster in the top right corner in *Umbrella* (Fig. 16).

To increase semantic and attention resolution, we increase $\lambda_{\hat{\mathbf{s}}}$'s dependency on finer layers to $\{4/9, 4/9, 1/9\}$. To deal with the boundary issues, we decrease the weight of fine layers towards the boundary back to $\{1/3, 1/3, 1/3\}$. The image boundary problem is resolved in *Umbrella* (Fig. 16). However, there is still a mismatch between the fidelity of the semantics and saliency (the head disappears in *Dynamic Face*), which is also reflected quantitatively (Tab. 8).

Thus, we use the same weight proportions and boundary reduction for both semantics and attention. This strikes a balance between correct edges from fine layers and whole object features from coarse layers, and mitigates the feature noise around image boundaries. This yields the best overall results both qualitatively on balance (Fig. 16) and quantitatively (Tab. 8).

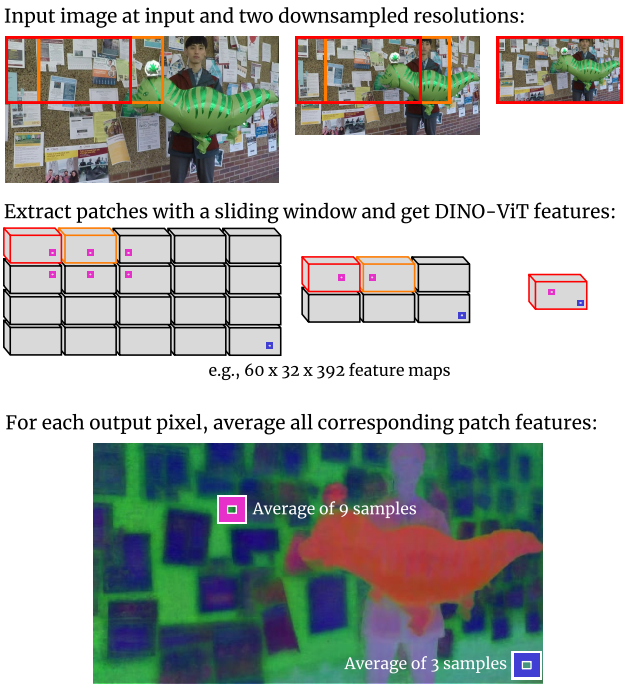

Figure 15: **Pyramid construction example.** This attempts to balance feature quality with computational cost by aggregating overlapping feature extraction blocks from different image resolutions.

Table 8: **Pyramid weighting choice.** Even though in our final algorithm the coarse layer has smaller weight, it balances high resolution edges from fine layers and whole object features from coarse layers while reducing geometry conflicts, and mitigate the feature noise around edges.
Metric: Adjusted Rand Index ($[-1, 1]$, higher is better).

	Input	Fix Cam 0	Fix Time 0
SAFF			
w/o pyr $\hat{\mathbf{s}}, \hat{\mathbf{a}}$	0.545	0.532	0.521
SAFF (ours)	**0.653**	**0.634**	**0.625**
w/ pyr $\lambda_{\hat{\mathbf{a}}} = \{1, 0, 0\}$	0.620	0.598	0.592
w/ pyr $\lambda_{\hat{\mathbf{a}}} = \{1, 0, 0\}$, $\lambda_{\hat{\mathbf{s}}} = \{1/3, 1/3, 1/3\}$	0.631	0.612	0.601

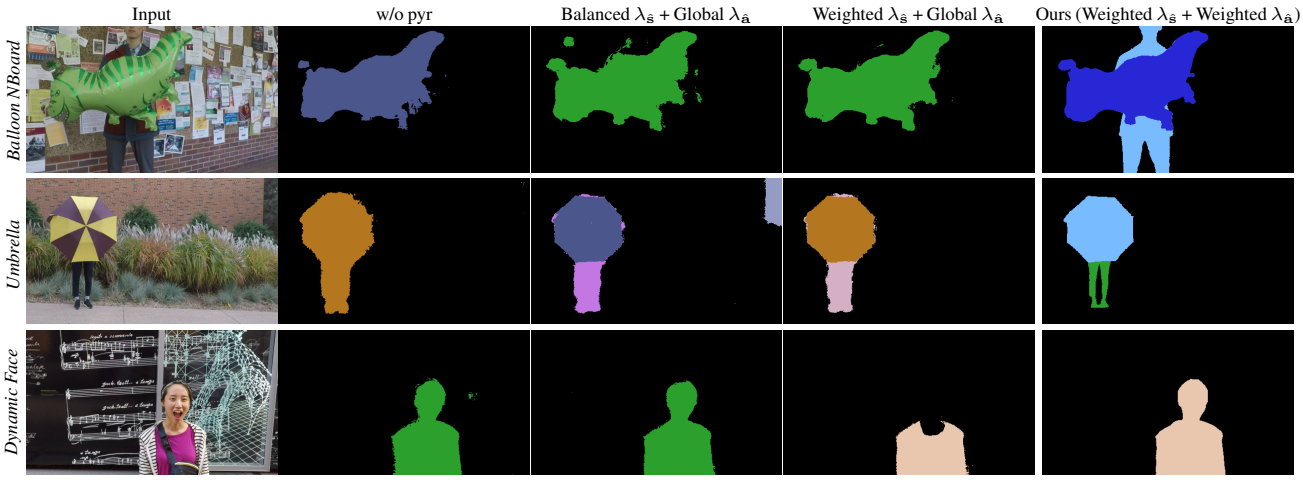

Figure 16: **Pyramid construction varies final output quality after clustering.** Without the pyramid, key objects are missing or undersegmented. Our approach captures the objects with fewest errors compared to the variants.
Balanced $\lambda_{\hat{s}}$ + Global $\lambda_{\hat{a}}$: $\lambda_{\hat{s}} = \{1/3, 1/3, 1/3\}$ with $\lambda_{\hat{a}} = \{1, 0, 0\}$
Weighted $\lambda_{\hat{s}}$ + Global $\lambda_{\hat{a}}$: semantic attention pyramid with $\lambda_{\hat{a}} = \{1, 0, 0\}$
Ours (Weighted $\lambda_{\hat{s}}$ + Weighted $\lambda_{\hat{a}}$): Our semantic attention pyramid

Algorithm 1 Pyramid Construction Algorithm (Example). Given an RGB image I of size $(H \times W \times 3)$ and a D-dimensional feature extractor $E : (A \times B \times 3) \mapsto ({}^{A}/_{4} \times {}^{B}/_{4} \times D)$, produce a processed feature map for the input image.

Input: $I \in R^{H \times W \times 3}$, $E \leftarrow dino\_vit8, H, W, D$
  $level0 \leftarrow I$
  $level1 \leftarrow$ DOWNSAMPLE$(I, 480, 256)$ ▷ Downsample image to 480×256.
  $level2 \leftarrow$ DOWNSAMPLE$(I, 240, 128)$
  $all\_patches\_in\_imagespace \leftarrow []$
  for $level \in [level0, level1, level2]$ **do**
    $x \leftarrow 0$
    while $x + 240 \leq W$ **do**
      $y \leftarrow 0$
      while $y + 128 \leq H$ **do**
        $patch \leftarrow level[y : y + 128, x : x + 240, :]$
        $feature\_patch \leftarrow$ UPSAMPLE$(E(patch), 240, 128)$
        $patch\_in\_imagespace \leftarrow$ NEW_NULL_ARRAY(H, W, D) ▷ To hold features in their input image location.
        $patch\_in\_imagespace[y : y + 128, x : x + 240, :] \leftarrow feature\_patch$
        $all\_patches\_in\_imagespace$.APPEND$(patch_in_imagespace)$
        $y \leftarrow y + 64$
      end while
      $x \leftarrow x + 64$
    end while
  end for
  $output\_full \leftarrow$ NON_NULL_AVERAGE$(all_patches_in_imagespace)$ ▷ Element-wise average of non-null values.
  $output \leftarrow$ PCA$(output_full, 64)$

E. Implementation Details

Semantics and Attention Following Amir *et al*. [1], for semantics we extract the 384-dim. 'key' facet from the 11^{th} layer of DINO-ViT, and for saliency we extract the 1-dim. 'attention' facet from the 11^{th} layer. For the pyramid, we use three levels. The coarsest level 0 is downsampled to 240×128. The finest level 2 is the input RGB size, with the mid level 1's size set between the two. For each level, we use DINO-ViT as a sliding window of size 240×128 to extract a (8×8 patch; stride 4) 60×32 feature map (i.e., level 0 has only one window position). For fast computation, we set window stride to 64. Once extracted, we upsample and place each feature map within level 2's frame. Then, for each pixel, we mean average all features from all windows that intersected it. Finally, to fit within GPU VRAM, we perform PCA on all images' normalized extracted pyramid $\hat{\mathbf{s}}, \hat{\mathbf{a}}$ features and keep the most important 64 dimensions.

Clustering Any clustering method has hyperparameters (or thresholds) for it to make decisions about cluster assignment. We use the same hyperparameters for all sequences.

We use the GPU via Faiss [15]. Again to fit within GPU VRAM, we uniformly sample every fifth point for elbow-k finding, then propagate cluster assignment to all points given k. We set the elbow-k threshold to 0.975 and the max cluster number to 25, with 10 trials per k. We cluster on direction and so normalize each pixel's vector.

Object extraction To extract an object from the volume, we sample 3D points along each input ray, then compare their semantics to to existing projected 2D semantic cluster centroids. We assign each 3D point to its closest centroid. Then, we set non-salient cluster label points to have zero density.

Post process All quantitative results are *without* this unless stated; only the main paper Table 3 line includes this. As appearance and geometry information is embedded in the volume, we want to refine the decomposition results by constraining them to align with rendered RGB and depth images. Specifically, we apply a CRF [20] with a pairwise Gaussian unary potential (θ_γ=3, w=15), a pairwise bilateral RGB potential (θ_γ=40, θ_β=13, w=10), and a pairwise bilateral depth potential (θ_γ=40, θ_β=13, w=20). Applying a CRF is similar to Amir et al. [1] on DINO-ViT in 2D, but our spacetime volume-integrated geometry provides a much stronger constraint on where the true edge is over time. The contribution of post processing is showed in Fig. 17 qualitatively. We see that small unimportant regions are removed, while still maintaining thin features and fine details. This trade-off is an application-level decision.

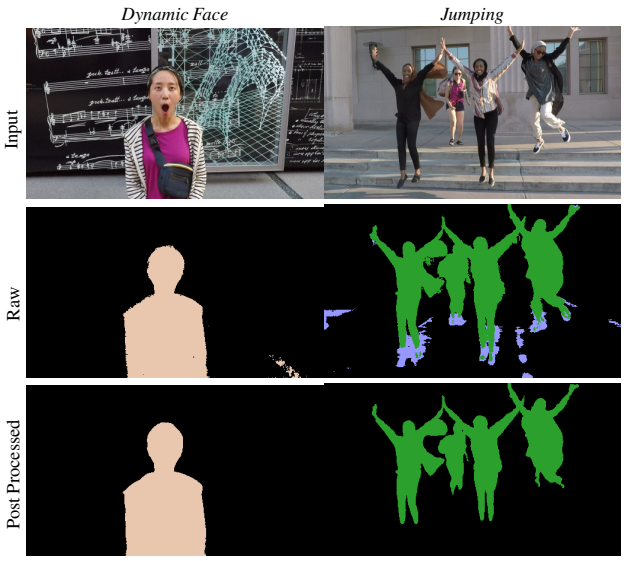

Figure 17: Post processing helps remove small noisy regions from the raw results while maintaining thin features.

Optimization routine and hyperparameters We optimize the combined loss with Adam optimizer, learning rate $5e^{-4}$, $\beta = (0.9, 0.999)$. We multiply prior losses for depth and optical flow by a decay rate. This rate starts at 1 and is divided by 10 at every $300{,}000^{\text{th}}$ iteration. For SAFF, we set reprojection losses $\lambda_{\hat{\mathbf{s}}_{i\to j}} = 1.0$ and $\lambda_{\hat{\mathbf{a}}_{i\to j}} = 1.0$, and prior losses $\lambda_{\hat{\mathbf{s}}} = 0.04$ and $\lambda_{\hat{\mathbf{a}}} = 0.04$ [18]. For all other losses, we follow Li et al. [22]: $\lambda_{|\mathbf{f}|} = 0.1$, $\lambda_{\delta\mathbf{f}} = 0.1$, $\lambda_{\hat{w}} = 0.1$, $\lambda_{\hat{\mathbf{c}}_{i\to j}} = 1.0$, $\lambda_{\text{Cyc}} = 1.0$, $\lambda_{\hat{d}} = 0.04$, $\lambda_{\hat{\mathbf{p}}} = 0.02$, $\lambda_{\text{entropy}} = 0.001$.

SAFF, its ablations, and NSFF are optimized for 360k iterations. As D^{2}NeRF is a different architecture, we use the author's stated 100k iterations.

Computational cost. The code was developed on Ubuntu 20.10 in Python/PyTorch, and trained on NVIDIA GeForce RTX 3090, NVIDIA GeForce RTX A6000, and NVIDIA GeForce RTX 2080 TI GPUs. All operations assume access to only 1 GPU. The CUDA VRAM required for using a trained SAFF on 540×288 image size is 12 GB, while optimization requires 24 GB. The CPU RAM used to optimize, cluster, and render SAFF used 16 GB, while we use 36 GB to extract objects. Optimizing a SAFF for $360,000$ iterations takes 1 to 2 days, depending on hardware, and is similar in time to NSFF. Recent improvements have dramatically reduced this time for non-semantic-attention fields [30, 7], and we expect similar performance gains were these methods used as the underlying architecture. In terms of runtime, we preprocess the DINO-ViT features and so do not incur significant additional cost during optimization, and none during inference due to DINO-ViT. Per-frame rendering is 15% slower than NSFF due to the additional heads. Saliency-aware clustering takes a few seconds only.

The computational cost is currently expensive, but we see our work as a step towards integrating high and low level information for 4D semantic volume reconstruction. NeRF-based approaches are still some way from real-time performance, but there have been significant gains recently (e.g., Instant-NGP [30]). Building our approach upon a fast backbone like this would make our approach more practical. One additional note is that, versus supervised 2D segmentation networks that are typically trained to be feed forward and to make predictions quickly (e.g., ProposeReduce takes only a few seconds to process a short sequence), the output of our model is richer as a 4D reconstruction with time-varying correspondence.

With respect to scalability, longer sequences will take more time to process, and at some point the capacity of the MLPs will limit reconstruction detail. For scenes with more dynamic elements, many objects are not in principle a problem, but instances that spatially overlap cannot be separately determined due to the fact that DINO-ViT features are not instance-aware.

Network architecture We add two heads to the architecture of NSFF [22]. For the semantic head, we add a single linear layer (256 neurons) appended by a tanh layer, with output dimension 64 to match the size of the per-sequence PCA-reduced DINO-ViT features. For the saliency head, we add a single linear layer (256 neurons) appended by a sigmoid layer, with output dimension 1.